Wiley Online Library
Early View publication on www.wileyonlinelibrary.com
(issue and page numbers not yet assigned;
citable using Digital Object Identifier – DOI)

J. Biophotonics 1–10 (2015) / **DOI** 10.1002/jbio.201500109

Journal of BIOPHOTONICS

FULL ARTICLE

Raman spectroscopy as a diagnostic tool for monitoring acute nephritis

Jingting Li[1], *Yong Du*[2], *Ji Qi*[1], *Ravikumar Sneha*[2], *Anthony Chang*[4], *Chandra Mohan*[2], *and Wei-Chuan Shih*[*, 1, 2, 3]

[1] Department of Electrical and Computer Engineering, USA
[2] Department of Biomedical Engineering, USA
[3] Department of Chemistry, University of Houston, 4800 Calhoun Rd. Houston TX 77204, USA
[4] Department of Pathology, The University of Chicago, USA

Received 6 February 2015, revised 15 April 2015, accepted 27 April 2015
Published online 22 May 2015

Key words: anti-glomerular basement membrane nephritis, acute nephritis, optical diagnosis, Raman spectroscopy, principal component analysis, linear discriminant analysis

Both acute nephritis and chronic nephritis account for substantial morbidity and mortality worldwide, partly due to the lack of reliable tools for detecting disease early and monitoring its progression non-invasively. In this work, Raman spectroscopy coupled with multivariate analysis are employed for the first time to study the accelerated progression of nephritis in anti-GBM mouse model. Preliminary results show up to 98% discriminant accuracy for the severe and midly diseased and the healthy among two strains of mice with different susceptibility to acute glomerulonephritis. This technique has the potential for non-invasive or minimally-invasive early diagnosis, prognosis, and monitoring of renal disease progression.

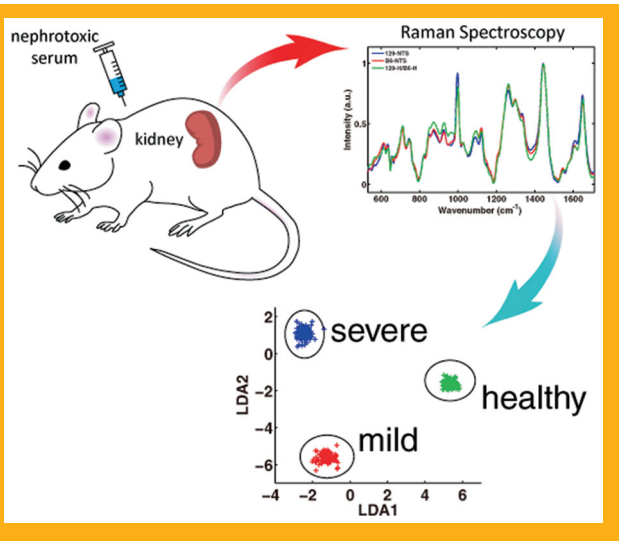

1. Introduction

Multiple underlying pathologies are known to precipitate acute nephritis or chronic nephritis, often leading to renal failure. These ailments are associated with considerable morbidity and mortality, largely due to the lack of good methodologies to diagnose nephropathies and monitor renal function effectively and non-invasively. Although renal biopsy may be useful in establishing diagnosis in several diseases, it is an invasive approach and impractical for longitudinal disease monitoring. Early detection and accurate diagnosis may avoid intensive immunosuppressive therapies and prevent irreversible renal da-

* Corresponding author: e-mail: wshih@uh.edu

mage in different renal diseases [1]. To this end, novel, non-invasive biomarkers are necessary to increase the accuracy and sensitivity of the diagnosis of renal inflammation, prognostic monitoring of response to treatment, and the detection of disease flares in various nephropathies.

Along this direction, different serum-based and urine-based biomarkers have been reported [2, 3]. In lupus nephritis (LN), for example, it has been reported that the composite marker of clinical variables and urine proteins such as urine monocyte chemoattractant protein-1 (uMCP-1), urine liver-type fatty acid–binding protein (uLFABP), urine hepcidin (uHepcidin), urine protein/creatinine ratio (uPCR) and serum creatinine (SCr) can be useful in reflecting specific pathologic lesions in LN patients [4]. Other than histopathology analysis, light-tissue interactions have shown promise for the diagnosis of various diseases in recent years [5–7]. Compared with biopsy and biomarkers, optical methods have the potential of developing non-invasive or minimally invasive and objective approaches in the assessment of pathological states [8]. Optical coherence tomography (OCT), visible and near-infrared diffuse spectroscopy and imaging, confocal imaging, dynamic spectral imaging, etc. have enabled new diagnostic methods in immunology, dermatology, diabetes, various cancers and so on. OCT allows for micrometer scale resolution images and noncontact examination. It is sensitive to structural features of the disease, but lack specificity in biochemical changes [9]. Diffuse reflectance spectroscopy has been used to quantify certain chemical components in bulk tissues by detecting changes in refractive index, but cannot detect changes from small sites, or determine the underlying biochemistry [10]. In contrast, Raman and infrared absorption spectroscopy are known to provide molecular fingerprints without any exogenous stains or labels [11]. In other words, they can detect and quantify subtle molecular or biochemical changes within the tissue. Unlike infrared absorption, Raman spectroscopy is particularly suited for biological tissue measurements because of its low sensitivity to water. The use of near-infrared (i.e., 700–950 nm) irradiation allows deep light penetration (~1 mm) into the tissue due to reduced scattering and water/chromaphore absorption.

Raman spectroscopy has been explored as a diagnostic and/or monitoring tool for different cancers [12–21], diabetes [22–27], cardiovascular diseases [28–30], cell and particle analysis [31–34] and other clinical indications. Optical biomarkers for glomerular diseases have been explored with the labeling of injured glomeruli with human monoclonal antibody F1.1 [35], however, the direct analysis of tissue constituents using quantitative or semi-quantitative Raman spectroscopy provides a methodology for non-invasive and label-free detection and evaluation of disease progression. With the help of plasmonic enhancement, surface-enhanced Raman scattering and spectroscopy have shown great potential in biomolecular sensing and imaging [22–23, 36–44].

Raman spectra obtained from biological samples often contain significant amounts of fluorescence background and the spectral differences between normal and diseased tissues are generally subtle. Also, Raman spectra contain various overlapping Raman bands. As a result, it is difficult to visually inspect and interpret the spectral data. Multivariate spectral analysis methods are often used to process the Raman spectra and facilitate data interpretation [12–13, 44–48]. Hence, we hypothesize that Raman spectroscopy with multivariate analysis can be an effective tool in the diagnosis of nephropathies as well.

Clinical studies of nephritis depend on both longitudinal and cross-sectional analysis of the medical history of hundreds of patients of various age, gender and ethnicity. While clinical studies over decades contribute to the study of pathology, the molecular process underlying LN is not well understood. A particularly useful approach for studying the molecular steps underlying LN is the experimentally induced anti-glomerular basement membrane (anti-GBM) model [49–51]. Among the different varieties of acute nephritis, anti-GBM disease or Goodpasture's disease is a relatively uncommon cause of glomerulonephritis when autoantibodies directed at specific antigenic targets within the glomerular or pulmonary basement membrane induce inflammation. Spontaneous lupus nephritis takes 6~12 months to manifest in mouse models, while the anti-GBM model can manifest in a quicker time frame.

In the mouse model of this disease, the abrupt exposure to "nephrotoxic" anti-GBM antibodies can compromise the recipient mice's renal function in a brisk and reproducible fashion. The severity of rapidly progressive glomerulonephritis is strain dependent. Depending on inbred genomes, different strains of mice exhibit differences in their susceptibility to immune-mediated nephritis and the resistance to spontaneously arising nephritis. The C57BL/6 (B6) and the 129/svJ (129) strain of mice are known for significant low and high susceptibility to anti-GBM disease, respectively, among 12 inbred strains of mice [52]. They are also relatively healthy and free of autoantibodies, which makes them suitable for the study by inducing nephritis. The use of this experimental model of acute nephritis has one added advantage. It may also be a useful model for studying the downstream pathways leading to chronic nephropathies such as LN.

In this work, we demonstrate that Raman spectroscopy combined with multivariate analysis can be a potential non-invasive diagnostic technique for nephritis in induced anti-GBM mouse model.

2. Methods

2.1 Mouse model

There were 2 strains of mice involved in the experiment, C57BL/6 (B6) and 129/svJ (129) (Jackson Laboratories, Bar Harbor, ME). Since females are more prone to the disease, all diseased mice were female. Between the two strains, B6 strains are less susceptible to nephritis, and the 129 strains are particularly sensitive to immune-mediated glomerulonephritis. GBM-reactive antibodies, referred to as "nephrotoxic serum" (NTS) was used to induce anti-GBM glomerulonephritis. Urine samples have been collected for 24 hr proteinuria test. All mice have been sacrificed at Day 14, and kidney tissue has been collected for histopathology and Raman spectroscopy analysis.

The spectra were measured from kidney samples from 41 anti-GBM-challenged and healthy mice of both strains, 8~10 weeks old. Among the 41 mice, 11 females were anti-GBM-challenged 129 mice (129-NTS), 14 females were anti-GBM-challenged B6 mice (B6-NTS), 7 females were healthy 129 mice (129-H), and 4 females and 5 males were healthy B6 mice (B6-H).

2.2 Data acquisition and pre-processing

Kidney samples were placed at the sample plane of a 785 nm laser line-scan Raman microscopy system [47]. A 133 μm × 1 μm laser line was projected on the medulla cross section. 133 Raman spectra were simultaneously acquired by a charge coupled device (CCD) camera in one frame of acquisition time 30 s at power density 3 mW/μm^2. From each kidney sample, multiple frames were acquired from 5~10 randomly chosen locations. Totally 476 frames consisting of 140 from 129-NTS, 145 from female B6-NTS, 94 from 129-H and 97 from B6-H were acquired.

The raw spectra were curvature corrected before binning across the entire CCD detector into one spectrum per frame, and smoothed to reduce noise [45]. A fifth order polynomial was used to approximate the spectroscopic background and subsequently removed [24, 25]. The dataset for the classifier consisted of Raman spectra in the range from 530 cm^{-1} to 1700 cm^{-1}.

2.3 Classification

After pre-processing, each spectrum was considered as one feature vector. The dimension of the feature vectors was first reduced by principal component analysis (PCA) or linear discriminant analysis (LDA), and then the new dataset consisting of dimensionality reduced feature vectors were used to build maximum likelihood (ML) classifiers [53–54]. Matlab software (Mathworks, MA) has been employed to perform data analysis.

Due to the limited number of samples, leave-one-out cross validation (LOOCV) and leave-one-mouse-out cross validation (LOMOCV) were employed to test the performance and accuracy of each classifier as a predictive model. Generally, leave-k-out cross validation is a rotational cross validation. The process aims to assess the performance of the classification model and acts as a simulation for prediction model with a limited dataset. In each round, k data points were used as testing data while the remaining data points were used as training data. For LOOCV, k equals one spectra. For LOMOCV, k represents all the spectra from one mouse. The process was repeated until each k spectra were used as testing data once. The classification results could be summarized in a classification matrix for each classifier.

Maximum likelihood (ML) estimation is a parametric classification method typically used after dimension reduction. ML estimates the parameters of a density that maximizes the likelihood of data under the assumption that the parameters are fixed and probability density function of the data set is known. Assuming the samples are drawn from a Gaussian distribution, the mean and the covariance matrix estimated by ML are the sample mean and the sample variances. The training data were used to construct n discriminate functions $g_i(x) = \ln p(x \mid C_i) + \ln P(C_i), \quad i = 1, 2, \ldots, n$, where x is a feature vector, and $P(C_i)$ are the likelihood and prior probability of class C_i respectively. The prior probability $P(C_i)$ was based on the number of samples involved in this experiment. Then the testing data were substituted into the discriminant functions and each feature vector was assigned a class accordingly. In a two class scenario, feature vector x is assigned to C_i if $g_i(x) > g_j(x),\ i \neq j$; here, the feature vector x is assigned to the class i with the largest $g_i(x)$ value.

3. Results

3.1 Proteinuria and renal pathology in anti-GBM-challenged mice

To ascertain the severity of induced nephritis, mice were monitored over 14 days for evidence of renal disease. As shown in Figure 1(a), the B6-NTS mice showed slightly elevated proteinuria levels under 5 mg/24 h, while the 129-NTS demonstrated signifi-

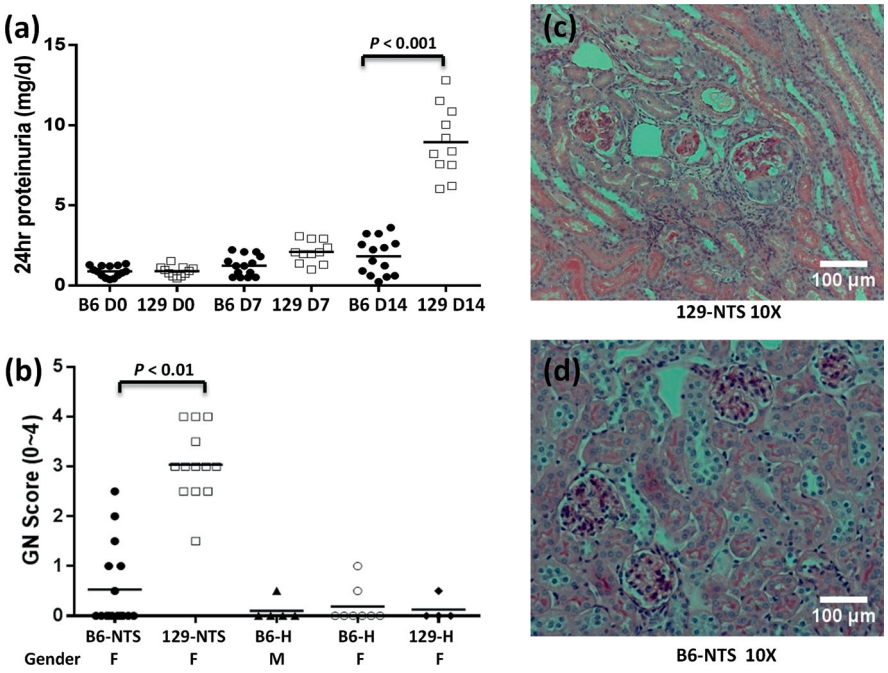

Figure 1 Proteinuria and renal pathology data. (**a**) Slightly increased proteinuria level in B6-NTS and significantly increased proteinuria level in 129-NTS. Each dot represents an anti-GBM-challenged mouse. D, day. (**b**) GN scores in all mice. F, female; M, male. (**c**), (**d**) Light-microscopic views (10×) of stained renal sections of histological nephritis and crescent formation in 129-NTS mice and B6-NTS mice.

cantly elevated proteinuria levels at day 14. Next, in the pathology study, 129-NTS exhibited the most severe glomerular disease with glomerulonephritis scores (GN scores) in the range 1.5~4 (typically grade 3) at day 14, as is shown in Figure 1(b). In contrast, the less susceptible B6-NTS only showed GN scores in the range of 0~2.5, whereas the control group of B6-H and 129-H exhibited no glomerulonephritis with GN score under 1. The anti-GBM-challenged mice also showed glomerular crescent formation as shown in the light-microscopic views of stained renal sections in Figure 1(c) and (d).

3.2 *Raman spectra with band assignment*

Figure 2 shows the average spectra from all 129-NTS, B6-NTS, 129-H and B6-H samples. All spectra were normalized to the largest peak [8, 13] at 1442 cm^{-1}. Dominant Raman bands can be observed among normal and diseased tissue corresponding to putative biochemicals such as phenylalanine at 1000 cm^{-1}, collagen at 1265 cm^{-1}, lipid at 1442 cm^{-1}, and Amide I at 1647 cm^{-1}. Raman bands are identified in the figure, with tentative band assignment shown in Table 1 [5, 13–16].

3.3 *Univariate analysis*

Before multivariate analysis, the peak of phenylalanine ring at 1000 cm^{-1} was used as a single feature to build a classifier. This peak shows a trend of decreasing peak height in the order of 129-NTS, B6-NTS and 129H/B6-H, as is shown in Figure 3. Here the peak intensity is calculated as the integration of area under peak. The intra-class variation is small compared to inter-class variation, and the inter-class p values between any two classes are less than 0.01.

The single peak intensity was used as the only feature in a ML classifier. Accuracy is the number of correctly classified feature vectors divided by the number of all feature vectors. The accuracy for the 1000 cm^{-1} peak intensity is only 59.45% for LOOCV and 54.41% for LOMOCV. A single peak intensity

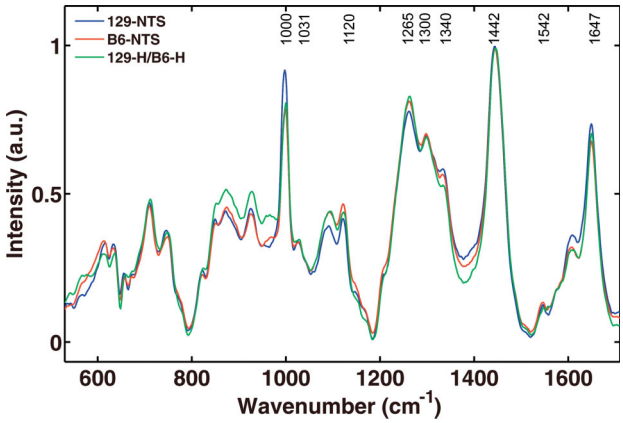

Figure 2 The average Raman spectra obtained from 129-NTS, B6-NTS, 129-H and B6-H samples are shown color-coded. Dominat Raman bands can be observed among normal and diseased tissue corresponding to putative biochemicals such as phenylalanine at 1000 cm^{-1}, collagen at 1265 cm^{-1}, lipid at 1442 cm^{-1}, and Amide I at 1647 cm^{-1}.

Table 1 Assignment of Raman bands.

Raman bands	Tentative assignments
600–900	Nucleic acid
1000	Phenyl ring breath (Amino acid, phenylalanine)
1031	C–H in-plane bending (phenylalanine)
1120	C–N stretch (protein backbone)
1265	Collagen, Amide III (protein)
1300	CH_2 bending mode, collagen wagging mode
1340	CH_2, CH_3 wagging (protein)
1442	Fatty acids, CH_2 (lipids and proteins)
1542	Single human RBC, Amide II (protein)
1647	Amide I (protein)

might be able to differentiate some classes only, as it represents only a small fraction of the spectra. From the results of the pathology study, it is expected that the nephritis in B6 mice would be less severe than that in 129 mice; correspondingly discrimination of this study group with precision may be particularly challenging, and it was incapable of being a sole indicator with high accuracy. Multivariate analysis was then used in order to utilize more information from the spectra instead of a single peak.

3.4 Multivariate, binary classification

We first show the classification of 3 pairs of datasets acquired from all female mice on the same day: (1) 129-NTS vs. B6-NTS, (2) 129-NTS vs. 129-H, and (3) B6-NTS vs. B6-H. In the PCA-ML analysis, the majority of information is usually retained in the largest principal components (PC), and there is inevitable information loss in dimensionality reduction. However, more information does not necessarily guarantee better accuracy. The performance is likely to fluctuate when involving more than a certain number of PCs and deteriorate with even more components. The number of PCs used was determined by the first maxima in accuracy while the cumulative weight is more than 90% to ensure a balance between the cost of computatition and a stable performance. For the LDA-ML classifier, linear discriminant (LD) components are the sorted eigenvalues of the multiplication of inter-class scatter and the inverse intra-class scatter. For N classes, the number of LDs equals $N - 1$, since the inter-class scatter is of rank $N - 1$ at most.

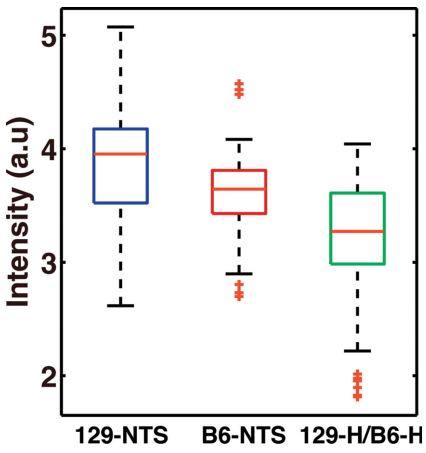

Figure 3 Box and whisker plot of the 1000 cm^{-1} peak intensity obtained from 129-NTS, B6-NTS and 129H/B6-H. Each group of box and whisker represents measurements from one group of mouse. The inter-class p values are less than 0.01.

Results in Table 2 show the summed confusion matrix of every cross validation test. In the confusion matrix, the diagonal elements are true positive predictions for each class, and non-diagonal elements are false positive predictions. Next, we use the following measurements to characterize the efficiency of the classifiers: sensitivity and precision. Sensitivity is the number of correctly classified samples divided by the number of actual positive samples in the data. Specificity is the number of correctly classified to other classes samples divided by the number of samples in all other classes. Precision is the number of correctly classified samples divided by the number of samples labeled as positive [55]. In Table 2, the PCA-ML accuracy for LOOCV and LOMOCV can generally reach >98% with the first 5~6 PCs with a cumulative weight of >90%. The B6-NTS and B6-H pair resulting in the same accuracy with 5 PCs for LOOCV and 9 PCs for LOMOCV respectively could be attributed to the mild condition of the disease in B6-NTS, so that the possibility of misclassified as healthy is higher than the severe condition of disease in 129-NTS. For such small datasets, the confusion matrices for LOOCV and LOMOCV are the same for each group, however, the cumulative PC weight is different in each case. For the LDA-ML classifier, the classification accuracy were all 100% and thus not shown in the table. These results demonstrate that our technique can successfully classify healthy vs. diseased and severe vs. mild in both strains without the confounding factor of either strain of gender.

Figure 4 shows the scatter plots of PCA and LDA. The statiscally most separable two PCs were plotted with each dataset, and 1-D scatter plots of LDs are ploted for all datasets. Figure 4 (i), (iv) are 129-NTS and B6-NTS, (ii), (v) are 129-NTS and 129-H, and (iii), (vi) are B6-NTS and B6-H. It could be seen that there is distinct difference between the spectra from the diseased and healthy mice, as well as between severe and mild conditions. For each dataset pair under the null hypothesis that the data come from the same distribution the p-values of the

Table 2 Confusion matrix of classification using PCA-ML.

LOOCV			
		Predicted classes	
		129-NTS	B6-NTS
Actual classes	129-NTS	47	0
	B6-NTS	1	39
Sensitivity		100%	
Specificity		97.50%	
6 PCs, weight = 92.87% accuracy = 98.85%			

LOOCV		
	Predicted classes	
	129-NTS	129-H
129-NTS	39	0
129-H	0	42
	100%	
	100%	
5 PCs, weight = 91.49% accuracy = 100%		

LOOCV		
	Predicted classes	
	B6-NTS	B6-H
B6-NTS	55	0
B6-H	1	48
	100%	
	97.96%	
5 PCs, weight = 97.10% accuracy = 99.04%		

LOOCV			
		Predicted classes	
		129-NTS	B6-NTS
Actual classes	129-NTS	47	0
	B6-NTS	1	39
		Sample classes	
		129-NTS	B6-NTS
Sensitivity		100%	
Specificity		97.50%	
6 PCs, weight = 93.06% acc = 98.85%			

LOOCV		
	Predicted classes	
	129-NTS	129-H
129-NTS	39	0
129-H	0	42
	Sample classes	
	129-NTS	129-H
	100%	
	100%	
5 PCs, weight = 91.07% acc = 100%		

LOOCV		
	Predicted classes	
	B6-NTS	B6-H
B6-NTS	55	0
B6-H	1	48
	Sample classes	
	B6-NTS	B6-H
	100%	
	97.96%	
9 PCs, weight = 97.10% accuracy = 99.04%		

first 3 PCs were all less than 0.05 and the null hypothesis is rejected.

Classification was also performed on 129-H and B6-H including both male and female mice. With 5 PCs, the accuracy could also reach 96.23% with 98.18% PC weight. However, the *p*-values of PC1, PC2 and PC3 were 0.77,0.48 and 0.07, respectively, indicating that they are statistically insignificance to reject the null hypothesis. The result prompted us to consider 129-H and B6-H as a single healthy class (129-H/B6-H) in the following analysis.

3.5 *Multivariate, multi-class classification*

Next we show the clasification efficacy on all three classes, i.e., healthy, mildly diseased, severely dis-

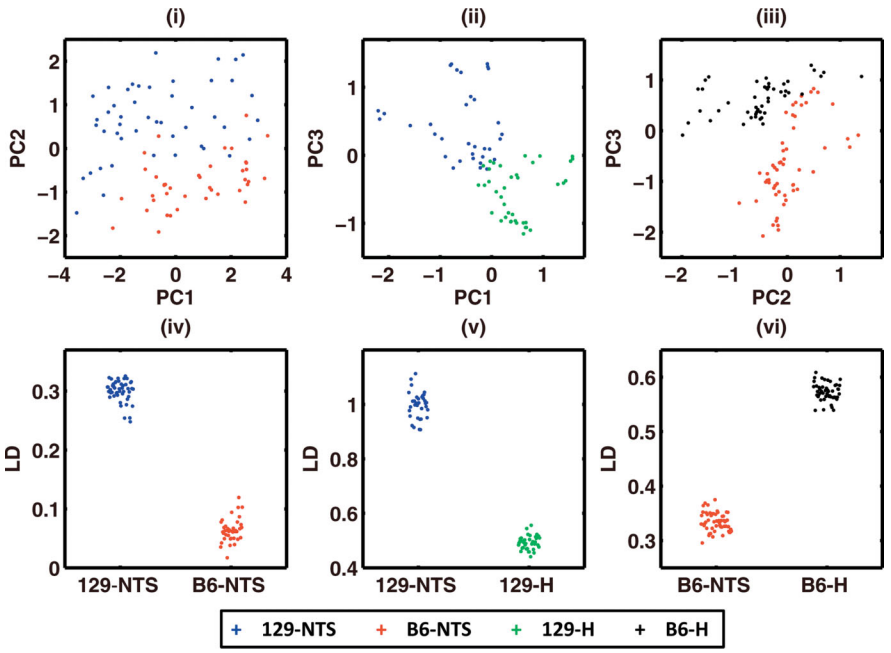

Figure 4 Scatter plots of PCA (first row) and LDA (second row). The statiscally most separable two PCs were plotted with each dataset, and 1-D scatter plots of LDs are ploted for all datasets. (i), (iv) are 129-NTS and B6-NTS; (ii), (v) are 129-NTS and 129-H; (iii), (vi) are B6-NTS and B6-H.

Table 3 Confusion and performance matrices of PCA-ML.

PCA-ML		Predicted classes (LOOCV)			Predicted classes (LOMOCV)		
		129-NTS	B6-NTS	129-H/B6-H	129-NTS	B6-NTS	129-H/B6-H
Actual classes	129-NTS	138	2	0	124	7	9
	B6-NTS	3	140	2	3	126	16
	129-H/B6-H	0	1	190	1	0	190
		Sample classes			Sample classes		
		129-NTS	B6-NTS	129-H/B6-H	129-NTS	B6-NTS	129-H/B6-H
Sensitivity		98.57%	96.55%	99.48%	88.57%	86.90%	99.48%
Precision		97.87%	97.90%	98.96%	96.88%	94.74%	88.37%
6 PCs (46.79%, 26.35%, 6.24%, 5.11%, 3.86%, 2.6%) total weight = 90.97% accuracy = 98.32%					13 PCs (61.19%, 14.86%, 6.50%, 3.94%, 2.95%, 2.40%, 1.74%, 1.49%, 0.99%, 0.71%, 0.56%, 0.40%, 0.35%) total weight =98.06 % accuracy =92.44 %		

eased. The results are shown Tables 3–4. Table 3 shows the summed confusion matrices of PCA-ML, including the precision and sensitivity. With LOOCV, the accuracy reached 98.32% with the first 6 PCs accounting for 90.97% cumulative weight. There was minimal overlapping among the classes, and no overlapping between 129-NTS and the healthy ones. With LOMOCV, 13 PCs of 98.06% weight only resulted in 92.44% accuracy, and the sensitivity of discriminating B6-NTS deteriorated the fastest when more samples were left out in the training step in LOMOCV than LOOCV. Table 4 shows the confusion matrices of LDA-ML and the summarized precision and sensitivity. The first two LDs had ~100% cumulative weight. The accuracy was 93.49% with LOOCV and 86.83% with LOMOCV. The separability between any two classes was not as pronounced as in PCA-ML. The difference of individual mice and the difference in meaurment conditions could have brought in variations that might not have been fully eliminated during the preprocessing and normalization. Especially for LOMOCV, the variations among individual mice were more influential to training a classifier during each round of cross validation since it might increase the intra-class variation while the inter-class difference is small.

Figure 5(a) shows the scatter plot of all data points as the training dataset for PCA. The depicted scatter plot using PC2 and PC3 is only for illustration purposes, though 6 or more PCs were used in the classifications. The three classes showed overlapping clusters with different centers. Figure 5(b) shows the LDA scatter plot with LD1 and LD2. The three clusters showed distinct clusters with no overlap. With LD1, the nephritis classes could be separated from the healthy class. With LD2, the three clusters could be separated from each other. However, when a testing datapoint falls into the intersection region of the three clusters, the probability of assigning it to any class would be comparable to each other, which increases the error rate. Figure 6 shows the PC loading spectra of PC1 through PC6

Table 4 Confusion and performance matrices of LDA-ML with 2 LDs.

LDA-ML		Predicted classes (LOOCV)			Predicted classes (LOMOCV)		
		129-NTS	B6-NTS	129-H/B6-H	129-NTS	B6-NTS	129-H/B6-H
Actual classes	129-NTS	138	1	1	132	7	1
	B6-NTS	8	132	5	15	126	4
	129-H/B6-H	3	13	175	19	18	164
		Sample classes			Sample classes		
		129-NTS	B6-NTS	129-H/B6-H	129-NTS	B6-NTS	129-H/B6-H
Sensitivity		98.57%	91.03%	91.62%	94.29%	86.90%	80.63%
Precision		92.62%	90.41%	96.69%	79.52%	83.44%	97.04%
2 LDs (56.79%, 43.21%) total weight = 100% accuracy = 93.49%					2 LDs (60.05%, 39.95%) total weight = 100% accuracy = 86.83%		

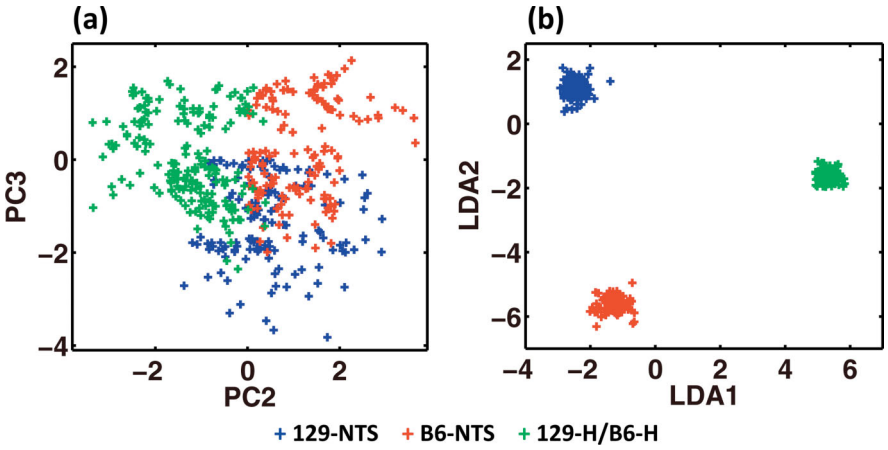

Figure 5 The scatter plots of PCA-ML and LDA-ML. (**a**) PCA-ML with PC2 and PC3; (**b**) LDA-ML with LD1 and LD2.

with more pronounced Raman bands indicated, which are phenylalanine at 1000 cm^{-1}, collagen at 1265 cm^{-1}, CH_2, CH_3 at 1340 cm^{-1}, lipid at 1442 cm^{-1} and Amide I at 1647 cm^{-1}. The prominent peaks in PC loadings indicate the weight of every wavenumber in each principal component, which is consistent with the previous observations of the averaged spectra.

4. Discussion

Among the different groups studied, B6-NTS exhibited the overall worst classification accuracy since the severity of disease in this group is between 129-NTS and healthy groups, and thus has the largest overlap with both classes. Since B6-NTS and the healthy groups have very similar GN scores, they exhibit more overlap than that between 129-NTS and B6-NTS, as observed in all datasets.

In the Raman spectra, the intensity variations of major peaks contribute to the majority of the variance, which is true for all classes. Since PCA linearly projects the original data to a new space to maximize data variance, it does not consider the separability of different classes. The largest eigenvectors of the covariance matrix are used as the transformation matrix to project the raw data into a dimension-reduced space. In this case, the contribution to the variances originate primarily from the prominent Raman bands, which caused overlapping, and the distribution of peak intensity cannot be fully distinguish among classes. In contrast, LDA achieves a linear projection of the original data to a new space by taking into account both the intra-class and inter-class distributions. In principle, it would reduce the overlap caused by contributions from the same peaks, and emphasize more on the peak difference between classes.

However, LDA does not always outperform PCA. Using the same number of components, the accumulation of PC weight will be much slower and smaller than LDA, and using 100% weight would defeat the purpose of dimensionality reduction and increase the computational cost. However, LDA can only produce at most features for a class problem, and there could be more information loss in the division of inter-class and intra-class scatters in LDA than diserting smaller PCs with PCA, especially when the underlying distribution is not known in advance [56].

5. Conclusion

In this work, we have demonstrated the efficacy of using Raman spectroscopy combined with multivariate analysis as a diagnostic tool for discriminating kidneys afflicted with acute nephritis from anti-

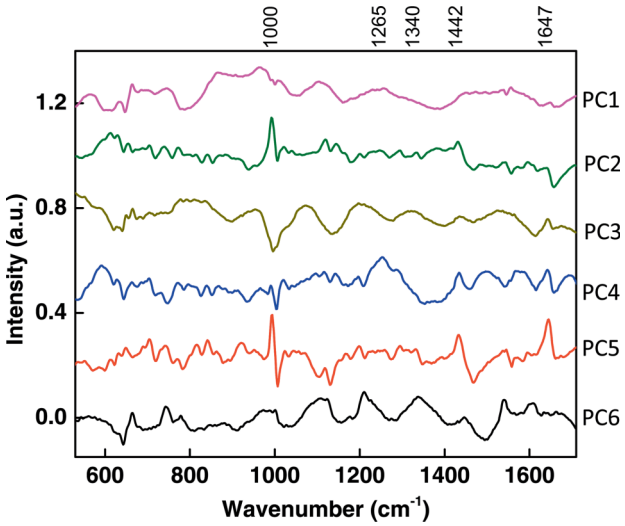

Figure 6 PC loading spectra of PC1 to PC6. More pronounced Raman bands such as phenylalanine at 1000 cm^{-1}, collagen at 1265 cm^{-1}, CH_2, CH_3 at 1340 cm^{-1}, lipid at 1442 cm^{-1} and Amide I at 1647 cm^{-1} are indicated.

GBM mosue models. Raman spectroscopy provides molecular fingerprints that enables non-invasive or minimal invasive and label-free detection for the quantification of subtle molecular changes. It has the potential to largely reduce the complexity in diagnosing and monitoring anti-GBM diseases. By adapting multivariate analysis to Raman spectroscopy, we have successfully differentiated between the diseased and the non-diseased with up to 100% accuracy, and among the severely diseassed, the mildly diseased and the healthy with up to 98% accuracy. Since the current study was carried out using isolated kidneys from mice with experimentally induced nephritis, it remains to be shown if this approach is equally powerful in mice with spontaneous nephritis, such as LN. Further optimization of the performance will be carried out in the future by implementing techniques that reduce or eliminate the effect of tissue turbidity [57]. Ultimately, Raman spectroscopy has the potential to provide non-invasive or minimally-invasive diagnosis and monitoring of pathological states.

Acknowledgements Wei-Chuan Shih acknowledges the National Science Foundation (NSF) CAREER Award (CBET-1151154), National Aeronautics and Space Administration (NASA) Early Career Faculty Grant (NNX12AQ44G) and a grant from Gulf of Mexico Research Initiative (GoMRI-030).

Author biographies Please see Supporting Information online.

References

[1] C. Fiehn, Y. Hajjar, K. Mueller, R. Waldherr, A. D. Ho, and K. Andrassy, Ann Rheum Dis **62**, 435–439 (2003).
[2] P. Devarajan, Curr Opin Pediatr **23**, 194–200 (2011).
[3] J. Reyes-Thomas, I. Blanco, and C. Putterman, Clin Rev Allergy Immunol **40**, 138–150 (2011).
[4] X. Zhang, H. N. Nagaraja, T. Nadasdy, H. Song, A. McKinley, J. Prosek, S. Kamadana, and B. H. Rovin, Kid Int **81**, 401–406 (2012).
[5] A. N. Bashkatov, E. A. Genina, V. I. Kochubey, and V. V. Tuchin, J Phys D: Appl Phys **38**, 2543–2555 (2005).
[6] J. T. Oh, M. L. Li, H. F. Zhang, K. Maslov, G. Stoica, and L. V. Wang, J Biomed Opt **11**, 34032 (2006).
[7] C. Zhu, G. M. Palmer, T. M. Breslin, F. Xu, and N. Ramanujam, J Biomed Opt **10**, 024032 (2005).
[8] C. Kendall, N. Stone, N. Shepherd, K. Geboes, B. Warren, R. Bennett, and H. Barr, J Pathol **200**, 602–609 (2003).
[9] C. A. Patil, N. Bosschaart, M. D. Keller, T. G. van Leeuwen, and A. Mahadevan-Jansen, Opt Lett **33**, 1135–1137 (2008).
[10] G. Zonios, L. T. Perelman, V. Backman, R. Manoharan, M. Fitzmaurice, J. Van Dam, and M. S. Feld, Appl Opt **38**, 6628–6637 (1999).
[11] D. I. Ellis and R. Goodacre, Analyst **131**, 875–885 (2006).
[12] U. Neugebauer, T. Bocklitz, J. H. Clement, C. Krafft, and J. Popp, Analyst **135**, 3178–3182 (2010).
[13] N. Stone, C. Kendall, N. Shepherd, P. Crow, and H. Barr, J Raman Spectrosc **33**, 564–573 (2002).
[14] Z. Zhuang, N. Li, Z. Guo, M. Zhu, K. Xiong, and S. Chen, J Biomed Opt **18**, 31103 (2013).
[15] A. Mahadevan-Jansen, M. F. Mitchell, N. Ramanujamf, A. Malpica, S. Thomsen, U. Utzinger, and R. Richards-Kortumt, Photochem Photobiol **68**, 123–132 (1998).
[16] Z. Huang, H. Lui, D. I. McLean, M. Korbelik, and H. Zeng, Photochem Photobiol **81**, 1219–1226 (2005).
[17] N. Sudheendran, J. Qi, E. D. Young, A. J. Lazar, D. C. Lev, R. E. Pollock, K. V. Larin, and W. C. Shih, Laser Phys Lett **11**, 105602 (2014).
[18] C. H. Liu, J. Qi, J. Lu, S. Wang, C. Wu, W. C. Shih, and K. V. Larin, J Innov Opt Health Sci (2014).
[19] A. S. Haka, K. E. Shafer-Peltier, M. Fitzmaurice, J. Crowe, R. R. Dasari, and M. S. Feld, P Natl Acad Sci USA, **102** 12371–12376 (2005).
[20] Z. Huang, A. McWilliams, H. Lui, D. I. McLean, S. Lam, and H. Zeng, Int J Cancer **107**, 1047–1052 (2003).
[21] S. Y. Feng, J. Q. Lin, Z. F. Huang, G. N. Chen, W. S. Chen, Y. Wang, R. Chen, and H. S. Zeng, Appl Phys Lett **102**, 043702 (2013).
[22] D. A. Stuart, J. M. Yuen, N. Shah, O. Lyandres, C. R. Yonzon, M. R. Glucksberg, J. T. Walsh, and R. P. Van Duyne, Anal Chem **78**, 7211–7215 (2006).
[23] K. Ma, J. M. Yuen, N. C. Shah, J. T. Walsh, M. R. Glucksberg, and R. P. Van Duyne, Anal Chem **83**, 9146–9152 (2011).
[24] W. C. Shih, K. L. Bechtel, and M. S. Feld, Handbook Of Optical Sensing Of Glucose In Biological Fluids And Tissues (CRC Press, 2008).
[25] W. C. Shih, K. L. Bechtel, and M. S. Feld, In Vivo Glucose Measurements, Vol. 174 (John Wiley & Sons, Inc., 2009).
[26] W. C. Shih, J Innov Opt Health Sci **8**, 1550022 (2015).
[27] W. C. Shih, K. L. Bechtel, and M. V. Rebec, J Biomed Opt **20**, 051036 (2015).
[28] P. R. Moreno, R. A. Lodder, K. R. Purushothaman, W. E. Charash, W. N. O'Connor, and J. E. Muller, Circulation **105**, 923–927 (2002).
[29] T. J. Römer, J. F. Brennan, M. Fitzmaurice, M. L. Feldstein, G. Deinum, J. L. Myles, J. R. Kramer, R. S. Lees, and M. S. Feld, Circulation **97**, 878–885 (1998).
[30] O. R. Scepanovic, K. L. Bechtel, A. S. Haka, W. C. Shih, T. W. Koo, A. J. Berger, and M. S. Feld, J Biomed Opt **12**, 064012 (2007).
[31] C. Xie, M. A. Dinno, and Y. Q. Li, Opt Lett **27**, 249–251 (2002).
[32] A. Nijssen, T. C. Bakker Schut, F. Heule, P. J. Caspers, D. P. Hayes, M. H. Neumann, and G. J. Puppels, J Invest Dermatol **119**, 64–69 (2002).

[33] J. W. Chan, D. S. Taylor, T. Zwerdling, S. M. Lane, K. Ihara, and T. Huser, Biophys J **90**, 648–656 (2006).
[34] J. Qi, J. Li, W. C. Shih, Biomed Opt Express **4**, 2376–2382 (2013).
[35] K. Chaudhary, D. T. Kleven, T. L. McGaha, and M. P. Madaio, Kidney Int **84**, 403–408 (2013).
[36] J. Qi, P. Motwani, J. Zeng, J. C. Wolfe, and W. C. Shih, Biomed Spectrosc Imaging **4**, 95–103 (2015).
[37] M. Li, F. Zhao, J. Zeng, J. Qi, J. Lu, and W. C. Shih, J Biomed Opt **19**, 111611 (2014).
[38] J. Qi, J. Zeng, F. Zhao, S. H. Lin, B. Raja, U. Strych, R. C. Willson, and W. C. Shih, Nanoscale **6**, 8521–8526 (2014).
[39] X. M. Qian and S. M. Nie, Chem Soc Rev **37**, 912–920 (2008).
[40] W. T. Lu, A. K. Singh, S. A. Khan, D. Senapati, H. T. Yu, and P. C. Ray, J Am Chem Soc **132**, 18103–18114 (2010).
[41] K. Kneipp, A. S. Haka, H. Kneipp, K. Badizadegan, N. Yoshizawa, C. Boone, K. E. Shafer-Peltier, J. T. Motz, R. R. Dasari, and M. S. Feld, Appl Spectrosc **56**, 150–154 (2002).
[42] J. B. Zeng, F. S. Zhao, J. Qi, Y. F. Li, C. H. Li, Y. Yao, T. R. Lee, and W. C. Shih, R Soc Chem Adv **4**, 36682–36688 (2014).
[43] X. Qian, X. H. Peng, D. O. Ansari, Q. Yin-Goen, G. Z. Chen, D. M. Shin, L. Yang, A. N. Young, M. D. Wang, and S. Nie, Nat Biotechnol **26**, 83–90 (2008).
[44] S. Feng, R. Chen, J. Lin, J. Pan, G. Chen, Y. Li, M. Cheng, Z. Huang, J. Chen, and H. Zeng, Biosens Bioelectron **25**, 2414–2419 (2010).
[45] J. Qi, K. L. Bechtel, W. C. Shih, Biomed Spectrosc Imaging, **3**, 359–368 (2014).
[46] G. R. Lloyd, L. E. Orr, J. Christie-Brown, K. McCarthy, S. Rose, M. Thomas, and N. Stone, Analyst **138**, 3900–3908 (2013).
[47] J. Qi, W. C. Shih, Appl Opt, **53**, 2881–2885 (2014).
[48] A. D. Ghanate, S. Kothiwale, S. P. Singh, D. Bertrand, and C. M. Krishna, J Biomed Opt **16**, 025003 (2011).
[49] Y. Fu, Y. Du, and C. Mohan, Clin Immunol **124**, 109–118 (2007).
[50] H. Lu, J. Zhen, T. Wu, A. Peng, T. Ye, T. Wang, X. Yu, N. D. Vaziri, C. Mohan, and X. J. Zhou, Am J Physiol Renal Physiol **299**, F445–452 (2010).
[51] D. C. Kluth and A. J. Rees, J Am Soc Nephrol **10**, 2446–2453 (1999).
[52] C. Xie, R. Sharma, H. Wang, X. J. Zhou, and C. Mohan, J Immunol **172**, 5047–5055 (2004).
[53] R. O. Duda, P. E. Hart, and D. G. Stork, Pattern Classification (Wiley, 2012).
[54] M. S. Pepe, The Statistical Evaluation of Medical Tests for Classification and Prediction (Oxford University Press, 2004).
[55] M. Sokolova and G. Lapalme, Inform Process Manag **45**, 427–437 (2009).
[56] A. M. Martínez and A. C. Kak, IEEE Trans: Pattern Anal Mach Intell **23**, 228–233 (2001).
[57] W. C. Shih, K. L. Bechtel, and M. S. Feld, Opt Express **16**, 12726–12736 (2008).